Multiscale processes controlling niobium mobility during supergene weathering

Quentin Bollaert, Mathieu Chassé, Thierry Allard, Alexandra Courtin, Laurence Galoisy, Gautier Landrot, Cécile Quantin, Delphine Vantelon, Georges Calas

Journal Pre-proofs

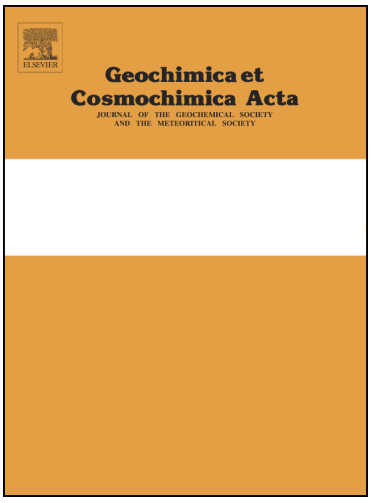

Multiscale processes controlling niobium mobility during supergene weathering

Bollaert Quentin, Chassé Mathieu, Allard Thierry, Courtin Alexandra, Galoisy Laurence, Landrot Gautier, Quantin Cécile, Vantelon Delphine, Calas Georges

PII: S0016-7037(23)00242-9
DOI: https://doi.org/10.1016/j.gca.2023.05.023
Reference: GCA 13066

To appear in: *Geochimica et Cosmochimica Acta*

Received Date: 30 November 2022
Revised Date: 20 February 2023
Accepted Date: 30 May 2023

Please cite this article as: Quentin, B., Mathieu, C., Thierry, A., Alexandra, C., Laurence, G., Gautier, L., Cécile, Q., Delphine, V., Georges, C., Multiscale processes controlling niobium mobility during supergene weathering, *Geochimica et Cosmochimica Acta* (2023), doi: https://doi.org/10.1016/j.gca.2023.05.023

Multiscale processes controlling niobium mobility during supergene weathering

Authors : Bollaert Quentin[1,*], Chassé Mathieu[1], Allard Thierry[1], Courtin Alexandra[2], Galoisy Laurence[1], Landrot Gautier[3], Quantin Cécile[2], Vantelon Delphine[3], Calas Georges[1].

*corresponding author

Affiliations :

[1]Sorbonne Université, Institut de Minéralogie, de Physique des Matériaux et de Cosmochimie, 4 place Jussieu, Paris, 75005, France

[2]Université Paris-Saclay, UMR 8148 GEOPS, 91405 Orsay Cedex, France

[3]Synchrotron SOLEIL, L'Orme des Merisiers, Saint-Aubin, BP 48 91192 Gif-sur-Yvette Cedex, France

ABSTRACT

Niobium (Nb) is one of the most immobile elements during supergene weathering, widely used for mass-balance calculations, despite elusive information on the mechanisms controlling its dynamics in the critical zone. Here, a multiscale approach, from weathering profile to atomic-scale, is developed to monitor Nb speciation along a thick (about 50 m) lateritic regolith formed over the Pitinga pluton (Amazonas, Brazil). In the A-type parent granite, Nb is mainly hosted in ilmenite (1.5–2 wt% Nb_2O_5) and, to a lesser extent, in rutile (2–3 wt% Nb_2O_5). A quantitative assessment of the average Nb speciation from the parent rock to the upper horizons has been carried out by combining spectroscopic and spatially-resolved chemical techniques. The contribution of Nb-bearing Ti oxides (2–6 wt% Nb_2O_5) and Fe oxides (0.1–0.3 wt% Nb_2O_5) in the average Nb speciation increases with the degree of weathering and reaches 80 % in the most altered horizon. This unusual Nb speciation results from the nature of the primary Nb carriers, less resistant to weathering than common Nb ore minerals such as pyrochlore. X-ray absorption spectroscopy demonstrates that Nb released from the weathering of ilmenite substitutes for Fe and Ti in goethite and Ti oxides, respectively, providing atomic-scale evidence of the high affinity of Nb for these phases. Elemental mobility of Nb, Ta and Sn followed by geochemical mass-transfer calculations evidences lateral transport from Nb-Sn-enriched laterites developed over the surrounding Nb-enriched facies of the Pitinga granite to the studied profile. Elements such as Ti, Zr and Hf, often considered immobile, are leached or redistributed in the studied profile. Our results demonstrate Nb remobilization during intense weathering. Although Nb scavenging by secondary Fe and Ti oxides limits Nb mobility at the mineral scale, this work questions the unrestricted use of Nb as a chemical invariant during surficial alteration processes.

Keywords : Niobium, supergene weathering, laterite, speciation, XANES spectroscopy, mass-balance calculations, elemental mobility

1. INTRODUCTION

Niobium (Nb) is among the most immobile elements during weathering processes (MacLean and Barrett, 1993) due to corrosion resistance of Nb-bearing minerals (McMaster et al., 2018) and low solubility in fluids (Peiffert et al., 2010). Such conservative behavior is essential to document geological processes (Hickmott and Spear, 1992; Ballouard et al., 2016) including mass-balance calculations of weathering budget (Nahon and Merino, 1996; Kurtz et al., 2000). Niobium immobility is at the origin of world-class deposits such as those found in Brazilian laterites, i.e. Araxá and Catalão Nb deposits, which represent about 90 % of the world production of this critical metal (U.S.G.S, 2022). Unparalleled Nb enrichment in laterites results from the tropical alteration of Nb-enriched carbonatite hosting weathering-resistant Nb phases from the pyrochlore supergroup minerals [$A_{2-x}B_2(O,OH)_6(OH,F,H_2O)_{1-y}$] (Mitchell, 2015). However, these Nb-enriched carbonatites are formed during complex multi-stage processes and, consequently, they are neither representative of typical carbonatite nor of the continental crust (Chakhmouradian, 2006).

In magmatic rocks, multicomponent Nb oxides are not the only Nb-bearing minerals. Widespread Ti oxides such as rutile, brookite and ilmenite are also typical hosts of Nb (Černý and Ercit, 1989). Niobium substitution for titanium (Ti) can reach high levels (30 wt% Nb_2O_5 in brookite and rutile and 15 wt% Nb_2O_5 in ilmenite) due to the vicinity of Nb and Ti ionic radii (Chakhmouradian and Mitchell, 1999; Ballouard et al., 2020). As titanium oxides are expected to be resistant to weathering (Milnes and Fitzpatrick, 1989; Meinhold, 2010), Nb should be preserved in these primary carriers and will remain immobile. However, the alteration of Ti oxides and ilmenite during intense chemical weathering in tropical regions has long been evidenced (Anand and Gilkes, 1984; Nahon and Merino, 1996; Du et al., 2012), questioning the fate of Nb after the dissolution of such minerals. Our understanding of Nb dynamics in supergene context is limited by the lack of data on Nb solubility and mobility in fluids (Lukyanova et al., 2017; Filella and May, 2020) and by the scarcity of studies identifying the evolution of Nb carriers during alteration of lithotypes distinct

from pyrochlore-bearing carbonatite. The study of Nb speciation in regoliths that formed at the expense of rocks containing Nb-bearing Ti oxides- and ilmenite allows to discuss Nb mobility in the critical zone.

In this study, we investigate Nb speciation in regolith samples from the region of the world-class tin (Sn)-Nb-tantalum (Ta) Pitinga deposit (Bastos Neto et al., 2009). Lateritic profiles formed from the weathering of the albite-enriched granite (Horbe and da Costa, 1999; Alves et al., 2018) exhibit exceptional Nb concentration (*ca* 1500 ppm Nb) due to the combination of singular magmatic and hydrothermal processes (Bastos Neto et al., 2009). Pyrochlore and columbite [$(Mn,Fe)Nb_2O_6$] from the parent rock have been preserved in the altered horizons despite the fragmentation of columbite into thin particles and the minor release of Nb from pyrochlore and columbite which was later incorporated into Fe oxides (Alves et al. 2018). Here, we complement the knowledge of the Pitinga province by studying Nb speciation in a laterite developed over the barren biotite alkali-feldspar granite (Lenharo et al., 2003). The investigation of this profile will uncover the processes of Nb concentration during supergene weathering that apply to widespread continental rocks and help discuss the role of the parent rock mineralogy.

2. Materials and Methods

2.1 Geological context and sampling

The Pitinga province is located within an A-type granitoid belt typical of extensional settings in the southern part of the Guiana shield, dated at 1.82 Ga (Bastos Neto et al., 2009; Bettencourt et al., 2016). As the Pitinga alluvial ore deposit is now exhausted, the Sn-Nb-Ta-enriched Pitinga granite is now mined for Sn, Nb and Ta. The studied lateritic profile (S0°44'52",W60°6'28") was sampled over the biotite–alkali feldspar Pitinga granite (1.822 ± 0.002 Ga) (Costi et al., 2000) exhibiting a moderate Nb enrichment (Fig. 1), more representative of granitic rocks than

surrounding highly-enriched facies characterized by a unique association of cryolite (Na_3AlF_6), Sn, Nb and several other rare metals (Bastos Neto et al., 2009).

The Pitinga region in the Amazon rainforest is characterized by a tropical-humid climate with intense rainfall (2000 mm · yr^{-1}) year-round, warm temperatures (*ca* 26 °C on average) and a long wet season (5–6 months). The lateritic cover is located on the summit of regional plateaus at *ca* 250 m elevation. In the region, they attain 50 m thick (Horbe and Da Costa, 1990; Alves et al., 2018). The minimum age assessed for such thickness is 1 Ma, considering an estimate of the progression of the weathering front at a rate of 0.05 mm · yr^{-1} in this region (Mathieu et al., 1995). Such long-term development of lateritic regolith is made possible by the elevation of the alteration profile providing protection from marine transgression events and by the stability of the latitude of the Amazon craton since 160 Ma, thus maintaining a tropical climate over the Cenozoic and part of the Mesozoic (Monteiro et al., 2018).

From the bottom to the top horizons, the studied regolith is composed of five units distinguished from their macroscopic properties: the granitic parent rock, the clayey mottled zone, the lateritic horizon, the bauxitic horizon and the ferruginous duricrust. Ten regolith samples, representative of these different horizons were collected from 3 to 50 m depth. The saprock and saprolite were not accessible at the outcrop and could not be sampled.

2.2 Bulk mineralogical characterization

X-ray diffraction was performed on powdered samples with a PANALYTICAL X'pert Pro MPD diffractometer. Measurements were carried out in Bragg-Brentano geometry using a Co Kα anode in order to minimize the X-ray absorption of Fe, enriched in the uppermost lateritic horizons. Data were recorded with an X'Celerator detector between 3 ° 2θ and 90 ° 2θ with 0.017 ° steps. Incident beam mask was fixed at 20 mm and Soller slits at 0.04 rad. Total counting time of measurement was 6 hours per sample. Identification and semi-quantification of the major mineral

phases were performed with X'Pert HighScore software. The accuracy of the mineralogical quantification is discussed in Supplementary Material (Table S1).

2.3 Bulk geochemical characterization

Two grams of powdered samples, representative of each horizon, were sent to the SARM (Service d'Analyses des Roches et des Minéraux, CRPG, Nancy) for chemical analysis (Table S2). Bulk concentrations of major and trace elements were analyzed by ICP–OES (iCap6500 ThermoFisher) and quadrupole ICP–MS (iVapQ ThermoFisher), respectively, after a lithium tetraborate alkali fusion (Carignan et al., 2001). Loss on ignition (L.O.I.) was obtained by gravimetric analysis at 1020 °C.

2.4 Mass-balance calculations

Quantification of the net chemical gains and losses was carried out using the following mass conservation equation (Brimhall et al., 1991).

$$\frac{V_p \rho_p C_{j,p}}{100} + m_{j,flux} = \frac{V_w \rho_w C_{j,w}}{100} \quad (1)$$

where V is the volume in cm^3, ρ is the dry bulk density (g/cm^3) and C is the concentration (wt%) of an element *j* in the parent material $C_{j,p}$ and in the weathered product $C_{j,w}$. The mass of an element *j* is denoted by the $m_{j,flux}$ term which is positive when an element *j* accumulates in the sample and negative when it is leached from the sample. In this work, we use the biotite granite from Pitinga as the parent rock in order to capture the chemical transfers due to lateritization processes. The use of thorium (Th) as the conservative element is further discussed.

Volumetric strain index ($\varepsilon_{i,w}$) corresponding to the volume change between the weathered material and the parent rock is estimated by :

$$\varepsilon_{i,w} = \left(\frac{\rho_p C_{i,p}}{\rho_w C_{i,w}}\right) - 1 \quad (2)$$

where ρ is the bulk density (g/cm^3) obtained by the paraffin method (Blake, 1965), $C_{i,p}$ and $C_{i,w}$ are the concentration of a reference element (considered as immobile during weathering) in the parent rock and weathered material, respectively. Volumetric strain around zero indicates isovolumetric weathering. Positive values indicate expansion and negative ones indicate collapse (Table S3).

Quantification of chemical mass gain or loss through a profile uses the open-system mass-transport function $\tau_{j,w}$ (Table S4), defined by :

$$\tau_{j,w} = \left(\frac{\rho_w C_{j,w}}{\rho_p C_{j,p}}\right)(\varepsilon_{i,w} + 1) - 1 \quad (3)$$

If $\tau_{j,w}$ is equal to 0, the element is immobile during weathering. A positive value reflects an absolute mass gain in element *j* of the weathered rock compared to the mass present in the parent rock whereas negative value indicates a mass loss. For instance, a positive value of 0.5 indicates that the mass of the element *j* results from an addition of 50 % relative to the mass of *j* present in the fresh parent rock.

2.5 Spatially-resolved chemical analyses

Polished sections of selected samples were made by impregnating chips in epoxy resin and polishing on cloth with diamond pastes.

Scanning electron microscopes (SEM) equipped with focused electron gun (FEG) (Zeiss Ultra55, Sorbonne Université and Zeiss Sigma, École Normale Supérieure, Paris) were used to map the polished sections with an AsB detector collecting backscattered electrons. The optimal working distance was chosen according to the geometry of the sample chamber and the beam energy fixed to 15.0 kV. Energy dispersive X-ray spectroscopy (EDS) chemical mapping was performed with a Bruker Quantax EDS system using an Oxford 50 mm^2 silicon drift detector (SDD).

Electron probe microanalysis (EPMA) was performed on a CAMECA SXFive EPMA equipped with five wavelength-dispersive spectrometers (WDS) at the Centre d'Analyse des Minéraux de Paris (CAMPARIS). An accelerating potential of 15 keV and a sample current of 40 nA have been used except for Fe oxides. Due to their small size and to protect them from beam radiation damage, the current was decreased to 15 nA. As a consequence, counting time was increased to analyze minor and trace elements such as Nb. Wavelength dispersive spectrometer analyses were performed using the following standards: Fe_2O_3 for iron (Fe), almandine for aluminum (Al) and silicon (Si), $MnTiO_3$ for manganese (Mn) and Ti, $NaNbO_3$ for Nb, metallic Ta for Ta, monazite for Th.

2.6 Reference compounds for X-ray absorption analyses

A large set of natural and synthetic Nb-bearing reference materials were considered as potential compounds for X-ray absorption near-edge structure (XANES) analyses (Bollaert et al., 2023). Apart from columbite-(Mn) and Nb-bearing ilmenite which were provided by École Nationale Supérieure des Mines de Paris (MINES ParisTech), Nb reference materials were synthesized in order to incorporate Nb concentrations representative of natural enrichment.

Niobium-substituted goethite was prepared by adapting a hydrothermal method used for Sc-bearing Fe oxides (Chassé et al., 2017). Niobium-substituted goethite was converted into Nb-substituted hematite (α-Fe_2O_3) by dehydroxylation. The synthesis of Nb-substituted anatase and rutile has been carried out using a sol-gel method at moderate temperature. Detailed mineral synthesis procedures are described in Bollaert et al. (2023). The synthesis of Nb-sorbed phases at concentrations representative of natural lateritic media could not be carried out because Nb oxides reprecipitation instantly before adsorption.

2.7 Procedures for synchrotron-based analyses

XANES data at Nb L_3- and K-edges have been collected at SOLEIL synchrotron facility (Saint-Aubin, France) operating with a storage ring current of 450 mA and energy of 2.75 GeV on the LUCIA (Vantelon et al., 2016) and SAMBA (Fonda et al., 2012) beamlines. The acquisition of spectra at the K and L_3-edges is complementary, since two similar spectra at the L_3-edge may be different at the K-edge, or inversely, since the information about the atomic-scale environment of Nb is different (Fig. S1).

A Si(111) double-crystal monochromator crystal was used on the LUCIA beamline with an energy resolution of 0.25 eV at 2400 eV (Schaefers et al., 2007). The monochromator was calibrated at the energy of the Nb L_3-edge using a Nb_2O_5 powder pellet. Due to high Nb contents in Nb mineralogical references, the spectra were recorded on cellulose-diluted pellets before being mounted on a sample-holder. The low penetration depth of X-rays at this energy or the low Nb contents required a data acquisition in the fluorescence mode. Energy steps were (2, 0.2, 1) eV for energy ranges of (2300–2350), (2350–2400) and (2400–2455) eV, respectively, with a 1 s integration time. Two measurements per sample at room temperature and under vacuum were sufficient to get adequate signal-to-noise ratio and check for reproducibility of the edge features.

Spatially resolved µ-XRF and µ-XANES analyses were conducted by focusing the beam with four total reflection mirrors in Kirkpatrick-Baez geometry. Micro-XRF element maps were carried out on polished sections using an energy dispersive–silicon drift diode (SDD). For each map, from 5 to 10 µ-XANES spectra of pre-identified minerals were recorded with an excitation energy of 2450 eV and a micro-beam focus of 2.8 x 3.8 µm.

Bulk Nb K-edge scans were collected from 18,700 to 20,000 eV using a continuous scan acquisition mode on the SAMBA beamline. The XANES region corresponds to the first 50 eV above the energy of the edge (*ca* 18,990-19,040 eV). The energy range for the EXAFS region is between the end of the XANES region up to 20,000 eV. The beamline was equipped with a Si(220)

monochromator providing a 2 x 0.5 mm (H x V) monochromatic beam. The samples were analyzed at 20 K using a He cryostat. Scans were obtained in 170 s and featured 1625 data points with a *ca* 0.8 eV step. Multiple scans were collected for each sample until no significant improvement in the signal-to-noise ratio of their merged spectra was observed. Up to 30 scans were collected for the bulk rock samples.

Normalization and least-squares linear combination fitting of X-ray absorption spectra were performed using Larch software (Newville, 2013).

3. RESULTS

3.1 Mineralogy and geochemistry

The biotite-alkali feldspar granite is a medium- to fine-grained leucocratic granite with a texture ranging from equigranular to porphyritic. It is composed of mesoperthitic alkali feldspar (Fig. 2a,b) (*ca* 53 %), albite (*ca* 33 %), quartz (*ca* 11 %) and biotite (*ca* 4 %) with chlorite, fluorite, zircon, monazite, ilmenite, rutile, apatite, xenotime, thorite, columbite, galena, cassiterite and barite, in order of abundance as characterized using SEM. Zircon, monazite, ilmenite and rutile are 10-20 µm large and found embedded in large biotite flakes (Fig. 2c), partially replaced by chlorite (Fig. 2d). Rutile also occurs as submicrometric grains within biotite. Thorite, apatite, monazite and cassiterite are found as isolated submicrometric crystal within feldspar. The alkali concentration of the granite in comparison to alumina concentration classifies it as a peraluminous granite. The concentration in high-field-strength elements (HFSE: i.e., zirconium (Zr), hafnium (Hf), Th, Nb, Ta, uranium (U) and rare-earth elements - REE) is *ca* 1200 ppm including *ca* 700 ppm of REE (Table S2). Niobium concentration is 46 ppm.

Above the parent granite, the lateritic profile consists of four distinct horizons (Fig. 3a). The clayey mottled zone exhibits pinkish (10R 8/4, from Munsell color chart, Soil Survey Staff, 2017)

and light red (2.5YR 7/6) colors with white clayey areas. The friable lateritic horizon is characterized by the predominance of reddish yellow matrix (5YR 7/8) composed of clays. A dark indurated bauxitic horizon (2.5YR 6/8) with white mottles is identified. The ferruginous duricrust (5YR 6/8) corresponds to a Fe-enriched crust containing consolidated nodules of Fe oxides (Fig. 3b, c).

The dominant mineral throughout the profile is kaolinite in variable proportions depending on the horizon (Fig. 3b). Gibbsite is found from the lateritic horizon up to the duricrust forming the top horizon and reaches a maximum in the bauxitic horizon (*ca* 45 wt%). Other minerals include quartz (5–13 wt%), Fe oxides (i.e., hematite and goethite, 2–11 wt%), anatase (2–3 wt%). Small amounts of rutile (< 1 wt%) are detected by XRD in the bauxitic horizon and the ferruginous duricrust. The proportion of Fe oxides increases from the bottom to the top of the profile (Fig. 3b). In the bauxitic horizon with the highest Zr content, zircon was also identified as a trace mineral on the XRD pattern (Fig. 3d).

The clayey mottled horizon is texturally similar to the lateritic horizon (Fig. 4a, b). Submillimetric grains of quartz are found along the profile (Fig. 4c). In the bauxitic horizon, kaolinite can be found as microcrystalline, forming stacks of lamellae discordant to the surrounding matrix (Fig. 4d). Iron oxides occur both as agglomerates of submicron size crystals (Fig. 4d) and as crystals of hundreds of microns isolated in the matrix in the lateritic horizon (Fig. 4b). Accessory minerals identified are zircon, Ti oxides, monazite, xenotime, thorite, columbite and cassiterite.

The bulk concentrations of major and minor elements reflect the mineralogical evolution. The Al_2O_3 and TiO_2 contents increase toward the surface with a maximum in the bauxitic horizon (41.5 and 1.0 wt%, respectively) and then slightly decrease in the ferruginous duricrust (Fig. 3c). The concentration of Fe_2O_3 increases up to 25 wt% in the duricrust while SiO_2 is depleted. The concentrations of Zr, Sn, Nb and Th increase from the bottom to the top of the laterite (Fig. 3d). The

concentration of REE in the laterite is below that of the granite and displays a complex evolution throughout the profile (Fig. 3d). The index of lateritization (IOL = 100 x[(Al_2O_3 + $Fe_2O_{3(T)}$) /(SiO_2+Al_2O_3+$Fe_2O_{3(T)}$)]) used to quantify the stage of chemical weathering of a sample (Babechuk et al., 2014) varies between 47 and 71 % from the bottom to the top of the profile. Using this index, the investigated profile is considered as kaolinitized to weakly lateritititized (Fig. 5a). The concentrations of HFSE such as Nb, Th, Zr are positively correlated (r = 0.81–0.99) with the IOL index (Fig. 5b).

The mobility of some HFSE and immobile elements were investigated in the profile considering Th as immobile (Fig. 6). Globally, the REE are lost throughout the profile (Fig. 6). The mass loss of most light REE (LREE) is strong in the entire profile (τ from -0.8 to -1.0) whereas the mass loss of heavy REE (HREE) and Y is weak to moderate in the bottom profile (τ from -0.3 to -0.6) and then reaches 0.8−0.9 of mass loss in the uppermost part of the profile (Table S4). The evolution of the mass fraction transport function τ for Zr and Ti is similar with a mass gain in the lower laterite followed by a continuous loss from -0.2 up to -0.7. Although the evolution of Hf and Zr is similar along the profile, the loss of Hf is lesser compared to Zr. (Fig. 6). On the scale of the profile, we note a moderate mass gain of Nb and Ta through the profile (τ = 0.1−0.7). Finally, we note a net gain of Sn of 1.0−2.0 relative to the parent rock with a maximum occurring in the ferruginous duricrust (τ = 2.8).

3.2 Identification and characterization of the niobium carriers

In the granitic parent rock, ilmenite is the main Nb-bearing phase. Ilmenite forms euhedral crystals of tens of micron isolated in millimetric biotite crystals (Fig. 7a, b). It is chemically characterized by high Mn and Nb concentrations (up to 10 wt % MnO and 2 wt % Nb_2O_5, Table 1). Niobium-bearing ilmenite (Fig. 7c) is replaced by another Nb-bearing Ti-Fe oxide (Fig. 7d). This mineral is presumably pseudorutile (Table 1) according to its Ti/(Fe+Ti) ratio, between 0.6 and 0.7,

and low totals obtained by microprobe analysis expected from its hydration (Grey et al., 1994). Alternatively, this phase could be a mixture between ilmenite and rutile. Micron-size crystals of Nb-bearing rutile also occur within the biotite matrix. Two types of Nb-bearing oxides occurring as trace minerals are also found. Micrometric Nb-bearing inclusions in ilmenite exhibiting preferential orientation (Fig. 7a) may be ascribed to fergusonite-(Y) or to Y-enriched columbite. Ferrocolumbite with slight enrichment in Sc is also identified (Fig. 7b).

In the altered horizons, based on chemical and textural differences, two types of Nb-bearing ilmenite (i.e. (i) preserved and (ii) altered ilmenite) and of Nb-bearing Ti oxides (i.e. (i) type-1 and (ii) type-2) are identifiable (Fig. 8). We found preserved Nb-bearing ilmenite in all the horizons. In the bauxitic horizon, Nb-bearing ilmenite are found within lamellae of kaolinite (Fig. 8a). Compared to the parent rock, Nb-bearing ilmenite is also manganoan but with a little less Mn (typically *ca* 5.0 wt% MnO) and with lower Nb concentrations (*ca* 1.0 wt % Nb_2O_5, Table 2). The replacement of Nb-bearing ilmenite by pseudorutile as observed in the granite (Fig. 7d) is not found in the laterite. Instead, some crystals can be described as pseudorutile surrounding an ilmenite core (Fig. 8b). Other ilmenite crystals display signs of alteration such as corrosion features and cracks (Fig. 8c,d). Although altered in all the horizons, the most evident signs of alteration of Nb-bearing ilmenite are observed in the bauxitic horizon.

Type-1 Nb-bearing Ti oxide with low amounts of Fe (*ca* 5 wt% Fe_2O_3) and without Mn is only observed in the bauxitic horizon. Significant amounts of Th observed on the EDS spectra of type-1 Ti oxide (*ca* 0.5 wt% ThO_2) may result from a substitution of Th for Ti (Gamaletsos et al., 2011). The presence of nanoscale Th-bearing inclusions in Ti oxide is also expected, as this Th for Ti substitution is limited by the large difference in ionic radii (1.0 and 0.61 Å). Thorium adsorption is excluded considering the low solubility of Th. The composition of these oxides could not be analyzed using EPMA due to their sub-micrometric size. Type-1 Ti oxide occurs as elongated

lamellae crystallizing between kaolinite sheets (Fig. 8e) and as poorly crystalline minerals surrounding kaolinite (Fig. 8f). Pure Nb-bearing Ti oxide is also observed (type-2 Ti oxide, Fig. 8 g, h). The crystals are larger than for type-1 Ti oxide (> 20 μm) and they contain more Nb than ilmenite (Table 2).

Micrometric size Fe oxides with low Nb contents (0.1–0.3 Nb_2O_5 wt%, Table 3) are also evidenced (Fig. 9a, b). The last Nb-bearing phase identified is columbite-(Mn) and -(Fe) (Table 4), found as fragmented grains (10–20 μm) within the kaolinite matrix (Fig. 9c). Columbite-(Fe) with low amounts of Sc is also found as inclusion in Nb-bearing ilmenite (Fig. 9d). The detection of Ti on the EDS spectrum may result from the interaction volume of the electron beam, larger than the columbite size (Fig. 9d). As for type-1 Ti oxide, the size of the inclusions of columbite prohibits an accurate determination of their composition, an EDS spectrum is shown instead (Fig. 9d). The qualitative evolution of Nb speciation along the regolith obtained by SEM observations is summarized in Table 5.

3.3 Characteristics of the X-ray absorption spectra of niobium carriers

The atomic environment of Nb in type-1 and type-2 Ti oxides, Fe oxides, ilmenite and columbite has been characterized using Nb L_3-edge micro-XANES spectroscopy and compared with spectra of mineral references (Bollaert et al., 2023).

The Nb XANES spectra of columbite (Fig. 10a) and Fe oxide (Fig. 10b) from Pitinga match those of the mineral references We find two distinct spectra between type-1 and type-2 Ti oxides. The position and intensity of the features of type-1 Ti oxide match the reference spectrum of Nb-bearing anatase considering the resolution of the spectra (Fig. 10c). The relative intensity of the features of type-2 Ti oxide spectrum better matches that of Nb-bearing rutile (Fig. 10d). As the spectra of mineral references match those of the Nb carriers from Pitinga, the reference spectra can

be used as components in the linear combination fitting procedure (Fig. 11,12). In absence of a reference for Nb-bearing ilmenite spectrum, we compare the spectrum of Pitinga ilmenite with Nb-bearing hematite and anatase in order to highlight the specificities of this spectrum (Fig. 10e). The micro-XANES spectrum of ilmenite being distinct from the other spectra, it will be further used as a fitting component.

3.4 Quantitative evolution of the average niobium speciation

A least-squares linear combination fitting procedure of Nb L_3- and K-edges XANES spectra on bulk samples was performed using spectra of relevant mineral references (Fig. 10, S1) to quantitatively follow the average Nb speciation along the profile (Fig. 11, 12).

The Nb L_3-edge spectrum of the clayey mottled horizon can be reproduced with the spectra of Nb-bearing ilmenite (60 %) and anatase (40 %), identified by SEM as the major Nb-bearing phases (Fig. 11). For the lateritic horizon, the combination of Nb-bearing ilmenite and Nb-bearing anatase spectra does not reproduce the L_3-edge spectrum (Fig. S2) and the addition of a 50% contribution of the spectrum of Nb-bearing Fe is required (Fig. 11). The result of the fit does not change depending on whether Nb-bearing hematite or goethite spectra is used due to their resemblance (Fig. 10b). In the bauxitic horizon, the contribution of Nb-bearing Fe oxides reaches 60 % (Fig. 11). Average Nb speciation derived from Nb L_3-edge XANES is summarized in Table 5.

The Nb XANES spectrum of the granite is only collected at the Nb K-edge due to low Nb concentration (45 ppm) preventing the acquisition of a spectrum with a good signal-to-noise ratio at the L-edge. The fit is not satisfactory with ilmenite and rutile reference spectra, which are the main Nb carriers in the granite according to SEM-EDS observations (Fig. S3). This discrepancy stems from major differences between the spectra of reference ilmenite and Pitinga ilmenite which was characterized by microanalysis (Fig. S4). The Nb K-edge XANES spectrum of Pitinga ilmenite has matching features in energy and relative intensity with the granite spectrum thus suggesting it is the

main Nb carrier (Fig. S4). The low signal-to-noise ratio of the μ-XANES spectrum of Pitinga ilmenite prevents the quantitative analysis of the Nb speciation of the granite (Fig. 12). In the following fits, the spectra of Nb-bearing rutile and anatase will be used to account for the proportions of Nb-bearing Ti oxides and ilmenite in absence of relevant Nb-bearing ilmenite spectrum. As a complement to the L_3-edge which allows determining the nature of the Ti oxides, the fit at the K-edge (Fig. 12) is thus used to distinguish the nature of the Nb-bearing Fe oxides, which have distinct spectra at the K-edge (Fig. S1). We obtain a satisfactory fit of the clayey mottled horizon spectrum only with Nb-bearing Ti oxides (60 % anatase and 40 % rutile). Like at the L_3-edge, the combination of Nb-bearing ilmenite and Ti oxides spectra does not reproduce the K-edge spectra of the lateritic and bauxitic horizons (Fig. S5). The best fit for the lateritic horizon spectrum is found when Nb-bearing goethite spectrum (50 %) is added to Nb-bearing Ti oxides (Fig. 12). In the bauxitic horizon, the fit with only Nb-bearing goethite and Ti oxides components fails to reproduce the features of the edge (Fig. S6). As ilmenite contributes less to the average Nb speciation in this horizon, this difference is more likely due to a missing component. The addition of 15 % of columbite, for which SEM-EDS analyses indicate increasing abundance in the top horizons (Fig. 9c), to 60 % goethite and 25 % anatase significantly improves the quality of the fit (Fig. 12). We also collected the Nb K-edge spectrum of the duricrust horizon which stands out by an intense pre-edge at ca. 18, 980 eV and a low intensity feature between the two main features (Fig. 12). This spectrum can only be fitted with a high proportion of columbite (50 %) and with Nb-bearing goethite (50 %). On average, Nb speciation obtained at the K-edge is consistent with that provided at the L_3-edge (Table 5).

4. DISCUSSION

4.1 Origin of the parent niobium mineralization

The Nb mineralization of the biotite granite from Pitinga is dominated by ilmenite and rutile with minor columbite (Fig. 7). The equilibrium temperature and pressure of formation of the granite were estimated to be 800–860 °C and 7.5 kbar (Lenharo et al., 2003). The Nb/Y value of the parent rock is typical of a A2-type granite indicating emplacement in post-collisional environment (Ferron et al., 2010). The low Nb/Ta ratio of the granite (*ca* 7) arises from the early crystallization of micas ($D_{Nb}/D_{Ta} = 2.00$) (Stepanov et al., 2014; Ballouard et al., 2016). The presence of ilmenite rather than magnetite indicates that the melt first evolved in reducing conditions (< Ni–NiO buffer, Ishihara, 1977). The formation of pseudorutile (Fig. 7d) is controlled by an increase of the oxygen fugacity of the magma body during its ascent, which increases the Fe^{3+}/Fe^{2+} ratio (Anand, 1984). This supports the hypothesis of Lenharo et al., (2003) suggesting that the biotite granite underwent partial crystallization followed by emplacement at shallow levels. Reduced Fe and Mn from the ilmenite structure are oxidized and released explaining the lower amount of Mn in pseudorutile (Schroeder et al., 2002).

At the late magmatic stage, the exsolution of a Y-rich Nb oxide from ilmenite, either fergusonite-(Y) or yttrocolumbite (Fig. 7d), is controlled by substitution of heterovalent cations other than Fe^{2+}, namely Mn^{2+}, Nb^{5+} and Ta^{5+} and by the oxidation state of Fe. The manganoan nature of ilmenite may have prevented greater incorporation of Nb due to the limited solubility of Nb in manganoan ilmenite at low temperature (Capitani, 2017). Despite its rarity, the presence of yttrocolumbite is likely as columbite has been reported in the studied biotite granite (Lenharo et al., 2003) and as inclusions in ilmenite (Beurlen and Thomas, 2006; Capitani, 2017). Similar orientation of exsolved phases may result from the crystallization process of columbite during exsolution which follows the crystallographic orientation of the octahedral chains of ilmenite (Capitani, 2017). The exsolution process may have concentrated Y and HREE explaining the formation of a Y-rich columbite.

4.2 Crystal-chemical and geochemical controls on niobium mobility in the critical zone

The combination of SEM (Fig. 8e, f) and XANES data (Fig. 11,12) demonstrates the alteration of ilmenite due to chemical weathering. Ilmenite can be resistant to supergene alteration (Berger et al., 2014; Janots et al., 2015) or prone to weathering (Mordberg et al., 2001; Du et al., 2012) depending on the geochemical conditions or on its crystal-chemistry. In oxidic weathering environment, Mn-rich ilmenite would be destabilized due to the possible formation of soluble Mn^{3+} and Mn^{4+} easing its weathering. In the studied profile, Nb speciation is therefore controlled by the capacity of alteration of primary ilmenite, releasing Nb in supergene fluids and leading to scavenging by secondary Fe and Ti oxides (Fig. 11,12).

Goethite is the main Nb-bearing Fe oxide as shown by the fit of K-edge XANES spectra of lateritic samples (Fig. 12, Fig. S7) and by crystal-chemistry of the Fe oxides (Table 3). The scavenging of Nb by Fe oxides is favored by the formation of goethite at the expense of hematite under cool and humid tropical climate with near-neutral pH fluids (Schwertmann, 1983; Kämpf and Schwertmann, 1983), in agreement with the expected conditions of alteration in the studied profile.

According to XRD results, anatase is the main Ti oxide in the profile but rutile is also detected in the bauxitic horizon and in the duricrust. The fingerprint analysis of type-1 and type-2 Ti oxides XANES spectra indicates they may be anatase and rutile, respectively (Fig. 10c, d). Type-2 Ti oxide is probably primary, inherited from the biotite granite. As Nb-bearing rutile component is not required in the fitting procedure (Fig. 11), the proportion of Nb hosted in rutile is likely minor at the scale of the profile.

4.3 Atomic-scale processes controlling niobium mobility during supergene weathering

Atomic-scale mechanisms of Nb incorporation into supergene phases will control the affinity of Nb for Ti and Fe oxides and Nb mobility after its release from ilmenite. They can be deduced

from the XANES signature of supergene Nb carriers (Fig. 10).

Goethite is a major host of Nb in the weathering profile (Table 5). Due to similar ionic radius ($^{[6]}Fe^{3+}$ = 0.645 Å and $^{[6]}Nb^{5+}$ = 0.64 Å, - Shannon, 1976) substitution between Nb^{5+} and Fe^{3+} is made possible by the formation of Fe vacancies ($5Fe^{3+}$ for $3Nb^{5+}$) which maintain charge balance (Bollaert et al., 2023). In goethite, the Nb^{5+}–Fe^{3+} substitution process could be accompanied by the loss of two H^+ occupying the tunnels between the double chains which would lead to the formation of $NbO_5(OH)$ octahedra. Although goethite from Pitinga incorporates only 0.1−0.3 % Nb_2O_5, goethite incorporating more than 1 % Nb_2O_5 has been reported in supergene environments (Wall et al., 1996 ; Melgarejo et al., 2012). Experimental studies have shown that goethite can accommodate up to 0.3 apfu (atom per formula unit) of Nb (Oliveira et al., 2008, 2009) but increasing Nb content leads to a decrease of the crystallinity due to the transformation of double octahedral chains into single ones as a result of the withdrawal of H atoms (Bolanz et al., 2013). The absence of Nb in hematite could be due to the limited affinity of Nb for this phase. Niobium ions would occupy face-sharing octahedra of the hematite structure leading to a strong electrostatic repulsion between cations (Bolanz et al., 2013).

The occurrence of Nb-adsorbed Fe oxides is unlikely at the concentrations found in goethite (*ca* 0.20 wt % Nb_2O_5) considering the low solubility of Nb (< 1.10^{-7} $mol.kg^{-1}$, Peiffert et al. 2010). The similarity of Nb-substituted goethite reference XANES spectrum with that of the Pitinga goethite also excludes the possibility of Nb adsorption onto Fe oxides. Such chemisorption process occurring onto hematite and goethite is nonetheless possible in near-neutral pH with 80−90 % of Nb being adsorbed (Ghosh et al., 2017) but only at extremely low Nb concentrations (*ca* 2.10^{-9} $mol.L^{-1}$).

The comparison between type-1 and type-2 Ti oxide XANES spectra with their respective reference counterparts (Fig. 10) gives access to the mechanisms of incorporation of Nb in Ti oxides. The significant shift of 0.5 eV of the second feature on type-1 Ti oxide XANES spectrum relative to

Nb-bearing anatase of reference mirrors distinct Nb environments (Fig. 10c).The presence of Fe in type-1 Ti oxide may ease Nb incorporation by a co-substitution of Nb^{5+} and Fe^{3+} for $2Ti^{4+}$ ($2Ti^{4+} = Fe^{3+} + Nb^{5+}$) and may prevent significant distortion of the local environment of Nb in type-1 Ti oxide. Such substitution, expected to occur in Nb-bearing Ti oxide from other laterites (Giovannini et al., 2020) is common in presence of high amounts of Fe such as it is the case in the studied profile. By contrast, the similarity between the spectra of type-2 Ti oxide and Nb-bearing rutile reference indicates similar Nb environment and therefore similar mechanisms of substitution. In absence of Fe, the incorporation of Nb results in the increased distortion of the Nb site and Nb−O distances (Bollaert et al., 2023). In this case, the incorporation of Nb is made possible by the formation of one Ti^{4+} vacancy for four Nb^{5+} which leads to the increase of Nb−O distances (Bollaert et al., 2023).

4.4 Selection of an immobile element for mass-balance calculations in the profile

The choice of the immobile element is a challenging task in mass-balance calculations as it is critical in determining element leaching or redistribution within the regolith and constraining biogeochemical cycles (Oh and Richter, 2005). In addition to Nb, typical elements chosen as immobile include Al, Ti, Zr, Hf, Ta (Grant, 2005; Szilas et al., 2016). However, the mineral carriers of these elements display signs of alteration in the studied profile. Ilmenite (Fig. 8c) and zircon (Fig. S6) are altered in the lateritic units making Ti, Zr and Hf unsuitable for such purpose. Tantalum, being carried by ilmenite, it cannot be used either. Given the textural characteristics of weathering-resistant cassiterite (SnO_2) found in the lateritic units (Fig. S6), Sn may be the least mobile element of the alteration profile. However, the use of Sn as a conservative element in mass-balance calculations leads to extreme mass loss of other relatively immobile elements (up to 90 % for Ti, Nb and Zr) which seems inconsistent with the relative abundance of Ti oxides and zircon. Such low values could be explained by an addition of Sn in the profile. The Sn concentration is 250 times

higher in the albite-enriched granite facies nearby than in the studied parent granite (Table S5). Even limited lateral transport of material from the laterite developed over the Sn-enriched granite would lead to a significant Sn mass gain in the studied laterite through a nugget effect. The use of Sn thus skews the results of mass-balance calculations leading to overestimation of elemental mass loss. Such lateral transport is evidenced mineralogically by the rare presence of Zr-enriched thorite (Fig. 9b) and columbite-(Mn) (Fig. 9c), absent in the parent rock but present in the surrounding enriched albite-enriched granite facies (Alves et al., 2018). As the profile is located on a slope downstream of the mineralized laterite (Fig. 1c), these minerals may have been brought in the form of solid particles to the studied profile by circulation of sub-surficial fluids or by mechanical sliding. Their occurrence is unlikely related to heterogeneities between the two granitic facies given the continuity of the geochemical data along the profile (Fig. 3c, d) and the absence of minerals typical of the albite-enriched granite (such as pyrochlore, columbite, cryolite) in the biotite granite.

Despite signs of monazite weathering mirrored by the mass loss of LREE (Table S4), the weak signs of alteration of thorite (Fig. S8) and the smaller difference in Th concentration between the studied parent rock and the neighboring albite-enriched granite (6-fold enrichment, Table S5), Th was chosen as the best conservative element for mass-balance calculations.

4.5 Assessment of Nb mobility at the scale of the profile

As evidenced by the weathering of ilmenite and further incorporation of Nb into Ti oxides and goethite, the remobilization of Nb at the micrometric scale implies potential mass loss of Nb at the scale of the profile which would result in τ_{Nb} close to 0 or slightly negative. Mass-balance calculations nonetheless indicate a moderate mass gain of Nb relative to the parent rock all along the profile (Fig. 6). Together with the contribution of columbite to Nb speciation in the bauxitic horizon and duricrust (Fig. 12), this supports the hypothesis of lateral transport. The importance of such lateral transport has been shown in laterites, where it affects directly the vertical evolution of trace

elements such as Ni and Sc along alteration profiles (Quesnel et al., 2017; Chassé et al., 2019). The very high contribution of columbite in the fit of the duricrust XANES spectrum could be due to a higher proportion of columbite in the analyzed powdered sample than in the rest of the sample. This nugget effect is corroborated by the τ_{Nb} value in the duricrust (0.24), lower than that of the bauxitic horizon (0.58).

Due to the *ca* 30-fold difference in the concentrations of Nb between the albite-enriched and biotite granite facies (Table S5), lateral transport masks potential losses of Nb due to supergene weathering and prevents to conclude on the mobilization of Nb at the profile scale. This may explain the absence of correlation between the index of lateritization (IOL) and the mass fraction transport function τ (Fig. 13a). Given the poor solubility of oxide species that Nb could form under the slightly acidic to near-neutral pH prevailing in laterites (Peiffert et al., 2010) and the affinity of Nb for supergene Fe and Ti oxides demonstrated by this study, Nb mobility is likely low and constrained to the scale of mineralogical assemblages. Along with this significant influence of pH on Nb speciation and therefore on Nb mobility, the effect of the presence of inorganic (sulphate, chloride, phosphate) and organic ligands remains to be explored (Friis and Casey, 2018)

4.6 Comparison with other 'immobile' elements

The behavior of other elements considered as immobile during supergene weathering was also studied. The study of Ta and Sn dynamics is hindered by mass gain resulting from lateral transport. The weak correlation obtained between the IOL index and τ for Ta (Fig. 13b) can be explained in the same way as for Nb because Ta, which is 30 times more enriched in the albite granite, substitutes for Nb in columbite which is transported to the studied profile. For Sn, the magnitude of τ is explained by lateral transport due the extreme differences in Sn concentration between the two source granites (by a factor of 250). The positive correlation showing that τ increases with the IOL index (Fig. 13c) and thus with depth (Fig. 5a), suggests that lateral transport

occurs in the entire profile and is more important in the top horizons. The negative correlations between the mass loss experienced by Ti (Fig. 13d), Zr (Fig. 13e) and Hf (Fig. 13f) and the IOL index evidence the increasing mobility of these elements with increasing degree of weathering. For these elements, lateral transport does not compensate the net mass loss induced by supergene weathering because the difference of concentrations between the biotite and albite facies is less significant (Table S5).

Several 'immobile' elements proved to be mobile in specific conditions of alteration (Braun et al., 2005). Titanium is mobile at the macroscopic scale due to intense weathering and complexation with organic matter (Cornu et al., 1999). Zirconium was found to be mobile in weathering profiles formed over rocks with alterable Zr-bearing silicates (Duvallet et al., 1999) but also with zircon which experienced metamictization (Balan et al., 2001). Intense and long-term alteration processes are responsible for a series of precipitation-dissolution reactions which induce Sc remobilization at least at the local scale (Chassé et al. 2019). Along with this study, possible mobility of 'immobile' elements shows that the choice of the best chemical invariant for mass-balance calculations must be a thought-out choice according to the conditions of formation of the studied profile and to the mineralogy of the source rock to accurately quantify element fluxes in the critical zone.

4.7 Influence of primary mineralization on Nb mobility

The role of the parent rock on the fate of Nb in the inherited lateritic profile is illustrated by the mineralogy of lateritic profiles resulting from the weathering of different granitic facies from Pitinga. These profiles formed within the same geodynamic context and under similar climatic conditions but over different granitic facies and distinct primary Nb-bearing phases. In the laterites formed from the albite-enriched facies, pyrochlore and columbite have been preserved despite the fragmentation of columbite into thin particles and the Nb released from pyrochlore and columbite

later incorporated secondary Fe oxides (Horbe and da Costa, 1999; Alves et al., 2018). The differences of Nb speciation in laterites from the Pitinga region are related to the diversity of primary Nb minerals in the parent rock. Lateritization processes will be more amenable to mobilize Nb from rocks containing Nb-bearing ilmenite and rutile than from rarer lithotypes bearing pyrochlore or columbite phases which are more resistant to supergene alteration.

CONCLUSION

The speciation of Nb along an entire lateritic regolith has been determined and quantitatively monitored with a multiscale approach combining SEM and EPMA microanalyses and XANESS data. The Nb mineralogy of the parent biotite granite, characterized by Ti-bearing oxides, i.e. ilmenite and rutile, is distinct from that encountered in the surrounding Nb-enriched Pitinga granites with complex multicomponent Nb oxides. Lateritization processes result in the formation of Nb-bearing Ti oxides (2−6 wt% Nb_2O_5) and goethite (0.1−0.3 wt% Nb_2O_5) at the expense of primary carriers in the altered horizons.

The mobility of Nb in the studied profile results from the alteration of primary Nb-bearing minerals which releases Nb in supergene fluids. However, the high affinity of Nb for Ti oxides and goethite, evidenced at the atomic-scale using XANES spectroscopy, limits the mobility of Nb to the scale of the mineralogical assemblage. Mass-balance calculations evidence a mass gain of Nb in the upper laterite which is explained by lateral transport of surrounding Sn-Nb-enriched laterite formed from the albite-enriched granite. XANES data show that this mass gain of Nb comes from a lateral transfer of columbite towards the studied profile, in parituclar in the upper horizons. An enrichment through lateral transport is also observed for Sn and Ta. By contrast, Zr, Hf and Ti, usually immobile, are leached in the studied profile.

The difference of Nb speciation in laterites from the Pitinga region is related to the diversity of primary Nb minerals with different degrees of resistance to weathering. The use of Nb as a chemical

invariant must be carefully considered as the mobility of Nb is dependent on the processes controlling primary Nb mineralization.

ACKNOWLEDGMENTS

The ANR RECA (ANR-17-CE01-0012) project and Adriana Horbe are acknowledged for providing samples for this study. Benoit Baptiste, Damien Deldicque, Ludovic Delbes and Imène Estève, as well as Michel Fialin and Nicolas Rividi from Sorbonne Université–CAMPARIS microprobe facility, are acknowledged for their help in sample preparation and analysis. We acknowledge SOLEIL for provision of synchrotron radiation beamtime and thank the staff of the LUCIA and SAMBA beamlines for their assistance in the measurement of Nb $L_{2,3}$-edges (Proposal No. 20191239) and K-edge spectra (Proposal No. 20200363). This work has been conducted in the framework of the PhD thesis of Q. Bollaert at ED398 GRNE, Sorbonne University.

RESEARCH DATA

Research Data associated with this article can be accessed at https://doi.org/10.5281/zenodo.7376789.

APPENDIX A. SUPPLEMENTARY MATERIAL

Supplementary material includes additional information on semi-quantitative analysis (Table S1), geochemical data (Table S2), mass-transfer calculations (Tables S3 and S4) and a comparison between the concentration of the biotite granite and the mineralized albite-enriched facies (Table S5). Supplementary figures show the Nb K-edge spectra of references (Fig. S1), comparison of spectra and tests of fits (Figs. S2, S3, S4, S5, S6, S7) and backscattered images of trace minerals more or less resistant to weathering (Fig. S8).

REFERENCES

Alves M. A. da S., Pereira V. P., Bastos Neto A. C. and Menegotto E. (2018) Weathering of the Madeira world-class Sn-Nb-Ta (Cryolite, REE, U, Th) deposit, Pitinga Mine (Amazon, Brazil). *J. Geochem. Explor.* 186, 61–76.

Anand R. R. (1984) Weathering of Ilmenite in a Lateritic Pallid Zone. *Clays Clay Miner.* 32, 363–374.

Anand R. R. and Gilkes R. J. (1984) Mineralogical and chemical properties of weathered magnetite grains from lateritic saprolite. *J. Soil Sci.* 35, 559–567.

Babechuk M. G., Widdowson M. and Kamber B. S. (2014) Quantifying chemical weathering intensity and trace element release from two contrasting basalt profiles, Deccan Traps, India. *Chem. Geol.* 363, 56–75.

Balan E., Neuville D. R., Trocellier P., Fritsch E., Muller J.-P. and Calas G. (2001) Metamictization and chemical durability of detrital zircon. *Am. Mineral.* 86, 1025–1033.

Ballouard C., Massuyeau M., Elburg M. A., Tappe S., Viljoen F. and Brandenburg J.-T. (2020) The magmatic and magmatic-hydrothermal evolution of felsic igneous rocks as seen through Nb-Ta geochemical fractionation, with implications for the origins of rare-metal mineralizations. *Earth-Sci. Rev.* 203, 103–115.

Ballouard C., Poujol M., Boulvais P., Branquet Y., Tartèse R. and Vigneresse J.-L. (2016) Nb-Ta fractionation in peraluminous granites: A marker of the magmatic-hydrothermal transition. *Geology* 44, 231–234.

Bastos Neto A. C., Pereira V. P., Ronchi L. H., de Lima E. F. and Frantz J. C. (2009) The world-class Sn, Nb, Ta, F (Y, REE, Li) deposit and the massive cryolite associated with the albite-enriched facies of the madeira a-type granite, Pitinga Mining District, Amazonas state, Brazil. *Can. Mineral.* 47, 1329–1357.

Berger A., Janots E., Gnos E., Frei R. and Bernier F. (2014) Rare earth element mineralogy and geochemistry in a laterite profile from Madagascar. *Appl. Geochem.* 41, 218–228.

Bettencourt J. S., Juliani C., Xavier R. P., Monteiro L. V. S., Bastos Neto A. C., Klein E. L., Assis R. R., Leite W. B., Moreto C. P. N., Fernandes C. M. D. and Pereira V. P. (2016) Metallogenetic systems associated with granitoid magmatism in the Amazonian Craton: An overview of the present level of understanding and exploration significance. *J. South Am. Earth Sci.* 68, 22–49.

Beurlen H. and Thomas R. (2006) Manganocolumbite and cassiterite exolsution lamellae in ilmenite from the Pitombeiras pegmatite (Acari - Rio Grande do Norte) in the Borborema pegmatitic province, NE-Brazil. 16, 3–15.

Blake G. R. (1965) Bulk Density. In *Methods of Soil Analysis* (ed. C. A. Black).

Bolanz R. M., Bläss U., Ackermann S., Ciobotă V., Rösch P., Tarcea N., Popp J. and Majzlan J. (2013) The Effect of Antimonate, Arsenate, and Phosphate on the Transformation of Ferrihydrite to Goethite, Hematite, Feroxyhyte, and Tripuhyite. *Clays Clay Miner.* 61, 11–25.

Bollaert Q., Chassé M., Elnaggar H., Juhin A., Courtin A., Galoisy L., Quantin C., Retegan M., Vantelon D. and Calas G. (2023) Niobium speciation in minerals revealed by $L_{2,3}$-edges XANES spectroscopy. *Am. Mineral.* doi: 10.2138/am-2022-8293.

Braun J.-J., Ngoupayou J. R. N., Viers J., Dupre B., Bedimo Bedimo J.-P., Boeglin J.-L., Robain H., Nyeck B., Freydier R., Nkamdjou L. S., Rouiller J. and Muller J.-P. (2005) Present weathering rates in a humid tropical watershed: Nsimi, South Cameroon. *Geochim. Cosmochim. Acta* 69, 357–387.

Brimhall G. H., Christopher J. L., Ford C., Bratt J., Taylor G. and Warin O. (1991) Quantitative geochemical approach to pedogenesis: importance of parent material reduction, volumetric expansion, and eolian influx in lateritization. *Geoderma* 51, 51–91.

Capitani G. C. (2017) Complex exsolution microstructures in ilmenite–pyrophanite from the Garnet Codera dyke pegmatite (Central Italian Alps): an electron microscopy investigation. *Mineral. Mag.* 81, 1087–1104.

Carignan J., Hild P., Mevelle G., Morel J. and Yeghicheyan D. (2001) Routine Analyses of Trace Elements in Geological Samples using Flow Injection and Low Pressure On-Line Liquid Chromatography Coupled to ICP-MS: A Study of Geochemical Reference Materials BR, DR-N, UB-N, AN-G and GH. *Geostand. Geoanalytical Res.* 25, 187–198.

Černý P. and Ercit T. S. (1989) Mineralogy of Niobium and Tantalum: Crystal Chemical Relationships, Paragenetic Aspects and Their Economic Implications. In *Lanthanides, Tantalum and Niobium* (eds. P. Möller, Petr Černý, and F. Saupé). Springer Berlin Heidelberg, Berlin, Heidelberg. pp. 27–79.

Chakhmouradian A. R. (2006) High-field-strength elements in carbonatitic rocks: Geochemistry, crystal chemistry and significance for constraining the sources of carbonatites. *Chem. Geol.* 235, 138–160.

Chakhmouradian A. R. and Mitchell R. H. (1999) Niobian ilmenite, hydroxylapatite and sulfatian monazite: alternative hosts for incompatible elements in calcite kimberlite from Internatsional'naya, Yakutia. *Can. Mineral.* 37, 1177–1189.

Chassé M., Griffin W. L., O'Reilly S. Y. and Calas G. (2019) Australian laterites reveal mechanisms governing scandium dynamics in the critical zone. *Geochim. Cosmochim. Acta* 260, 292–310.

Chassé M., Griffin W. L., O'Reilly S. Y. and Calas G. (2017) Scandium speciation in a world-class lateritic deposit. *Geochem. Perspect. Lett.*, 105–114.

Cornu S., Lucas Y., Lebon E., Ambrosi J. P., Luizão F., Rouiller J., Bonnay M. and Neal C. (1999) Evidence of titanium mobility in soil profiles, Manaus, central Amazonia. *Geoderma* 91, 281–295.

Costi H. T., Dall'agnol R. and Moura C. A. V. (2000) Geology and Pb-Pb Geochronology of Paleoproterozoic Volcanic and Granitic Rocks of Pitinga Province, Amazonian Craton, Northern Brazil. *Int. Geol. Rev.* 42, 832–849.

Du X., Rate A. W. and Gee M. A. M. (2012) Redistribution and mobilization of titanium, zirconium and thorium in an intensely weathered lateritic profile in Western Australia. *Chem. Geol.* 330–331, 101–115.

Duvallet L., Sabatier U. P. and Jules-Guesde A. (1999) The mobility of zirconium and identification of secondary Zr-bearing phases in bauxite from Poços de Caldas, Minas Gerais, Brazil: A mass-balance and X-ray absorption spectroscopic study. *Can. Mineral.* 37, 635–651.

Ferron J. M. T. M., Bastos Neto A. C., Lima E. F., Nardi L. V. S., Costi H. T., Pierosan R. and Prado M. (2010) Petrology, geochemistry, and geochronology of Paleoproterozoic volcanic and granitic rocks (1.89–1.88 Ga) of the Pitinga Province, Amazonian Craton, Brazil. *J. South Am. Earth Sci.* 29, 483–497.

Filella M. and May P. M. (2020) The aqueous solution thermodynamics of niobium under conditions of environmental and biological interest. *Appl. Geochem.* 122, 104729.

Fonda E., Rochet A., Ribbens M., Barthe L., Belin S. and Briois V. (2012) The SAMBA quick-EXAFS monochromator: XAS with edge jumping. *J. Synchrotron Radiat.* 19, 417–424.

Friis H. and Casey W. H. (2018) Niobium Is Highly Mobile As a Polyoxometalate Ion During Natural Weathering. *Can. Mineral.* 56, 905–912.

Gamaletsos P., Godelitsas A., Mertzimekis T. J., Göttlicher J., Steininger R., Xanthos S., Berndt J., Klemme S., Kuzmin A. and Bárdossy G. (2011) Thorium partitioning in Greek industrial bauxite investigated by synchrotron radiation and laser-ablation techniques. *Nucl. Instrum. Methods Phys. Res. Sect. B Beam Interact. Mater. At.* 269, 3067–3073.

Ghosh M., Swain K. K. and Verma R. (2017) Interaction of niobium with iron-oxide colloids and the role of humic acid. *J. Environ. Radioact.* 178–179, 101–109.

Giovannini A. L., Mitchell R. H., Bastos Neto A. C., Moura C. A. V., Pereira V. P. and Porto C. G. (2020) Mineralogy and geochemistry of the Morro dos Seis Lagos siderite carbonatite, Amazonas, Brazil. *Lithos* 360–361, 105433.

Grant J. A. (2005) Isocon analysis: A brief review of the method and applications. *Phys. Chem. Earth Parts ABC* 30, 997–1004.

Grey I. E., Watts J. A. and Bayliss P. (1994) Mineralogical nomenclature: pseudorutile revalidated and neotype given. *Mineral. Mag.* 58, 597–600.

Hickmott D. and Spear F. S. (1992) Major-and Trace-Element Zoning in Garnets from Calcareous Pelites in the NW Shelburne Falls Quadrangle, Massachusetts: Garnet Growth Histories in Retrograded Rocks. *J. Petrol.* 33, 965–1005.

Horbe A. M. C. and da Costa M. L. (1999) Geochemical evolution of a lateritic Sn–Zr–Th–Nb–Y–REE-bearing ore body derived from apogranite: the case of Pitinga, Amazonas — Brazil. *J. Geochem. Explor.* 66, 339–351.

Ishihara S. (1977) The magnetite-series and ilmenite-series granitic rocks. *Min. Geol.* 27, 293–305.

Janots E., Bernier F., Brunet F., Muñoz M., Trcera N., Berger A. and Lanson M. (2015) Ce(III) and Ce(IV) (re)distribution and fractionation in a laterite profile from Madagascar: Insights from in situ XANES spectroscopy at the Ce L_{III}-edge. *Geochim. Cosmochim. Acta* 153, 134–148.

Kämpf N. and Schwertmann U. (1983) Goethite and hematite in a climosequence in southern Brazil and their application in classification of kaolinitic soils. *Geoderma* 29, 27–39.

Kurtz A. C., Derry L. A., Chadwick O. A. and Alfano M. J. (2000) Refractory element mobility in volcanic soils. *Geology* 28, 683–686.

Lenharo S. L. R., Pollard P. J. and Born H. (2003) Petrology and textural evolution of granites associated with tin and rare-metals mineralization at the Pitinga mine, Amazonas, Brazil. *Lithos* 66, 37–61.

Lukyanova E. V., Akinfiev N. N., Zotov A. V., Rass I. T., Kotova N. P. and Korzhinskaya V. S. (2017) Niobium in hydrothermal systems related to alkali granites: Thermodynamic description of hydroxo and hydroxofluoride complexes. *Geol. Ore Depos.* 59, 305–314.

MacLean W. H. and Barrett T. J. (1993) Lithogeochemical techniques using immobile elements. *J. Geochem. Explor.* 48, 109–133.

Mathieu D., Bernat M. and Nahon D. (1995) Short-lived U and Th isotope distribution in a tropical laterite derived from granite (Pitinga river basin, Amazonia, Brazil): Application to assessment of weathering rate. *Earth Planet. Sci. Lett.* 136, 703–714.

McMaster S. A., Ram R., Faris N. and Pownceby M. I. (2018) Radionuclide disposal using the pyrochlore supergroup of minerals as a host matrix—A review. *J. Hazard. Mater.* 360, 257–269.

Meinhold G. (2010) Rutile and its applications in earth sciences. *Earth-Sci. Rev.* 102, 1–28.

Melgarejo J. C., Costanzo A., Bambi A. C. J. M., Gonçalves A. O. and Neto A. B. (2012) Subsolidus processes as a key factor on the distribution of Nb species in plutonic carbonatites: The Tchivira case, Angola. *Lithos* 152, 187–201.

Milnes A. R. and Fitzpatrick R. W. (1989) Titanium and Zirconium Minerals. In *Minerals in Soils Environments(2nd edition)* (eds. J. B. Dixon and S. B. Weed). pp. 1031–1206.

Mitchell R. H. (2015) Primary and secondary niobium mineral deposits associated with carbonatites. *Ore Geol. Rev.* 64, 626–641.

Monteiro H. S., Vasconcelos P. M. P., Farley K. A. and Lopes C. A. M. (2018) Age and evolution of diachronous erosion surfaces in the Amazon: Combining (U-Th)/He and cosmogenic 3He records. *Geochim. Cosmochim. Acta* 229, 162–183.

Mordberg L. E., Stanley C. J. and Germann K. (2001) Mineralogy and geochemistry of trace elements in bauxites: the Devonian Schugorsk deposit, Russia. *Mineral. Mag.* 65, 81–101.

Nahon D. and Merino E. (1996) Pseudomorphic replacement versus dilation in laterites: petrographic evidence, mechanisms, and consequences for modelling. *J. Geochem. Explor.* 57, 217–225.

Newville M. (2013) Larch: An Analysis Package for XAFS and Related Spectroscopies. *J. Phys. Conf. Ser.* 430, 012007.

Oh N.-H. and Richter D. D. (2005) Elemental translocation and loss from three highly weathered soil–bedrock profiles in the southeastern United States. *Geoderma* 126, 5–25.

Oliveira L. C. A., Ramalho T. C., Souza E. F., Gonçalves M., Oliveira D. Q. L., Pereira M. C. and Fabris J. D. (2008) Catalytic properties of goethite prepared in the presence of Nb on oxidation reactions in water: Computational and experimental studies. *Appl. Catal. B Environ.* 83, 169–176.

Oliveira L. C. A., Zaera F., Lee I., Lima D. Q., Ramalho T. C., Silva A. C. and Fonseca E. M. B. (2009) Nb-doped hematites for decomposition of isopropanol: Evidence of surface reactivity by in situ CO adsorption. *Appl. Catal. Gen.* 368, 17–21.

Peiffert C., Nguyen-Trung C., Palmer D. A., Laval J. P. and Giffaut E. (2010) Solubility of B-Nb_2O_5 and the Hydrolysis of Niobium(V) in Aqueous Solution as a Function of Temperature and Ionic Strength. *J. Solut. Chem.* 39, 197–218.

Quesnel B., de Veslud C. L. C., Boulvais P., Gautier P., Cathelineau M. and Drouillet M. (2017) 3D modeling of the laterites on top of the Koniambo Massif, New Caledonia: refinement of the per descensum lateritic model for nickel mineralization. *Miner. Deposita* 52, 961–978.

Schaefers F., Mertin M. and Gorgoi M. (2007) KMC-1: A high resolution and high flux soft x-ray beamline at BESSY. *Rev. Sci. Instrum.* 78, 123102.

Schroeder P. A., Le Golvan J. J. and Roden M. F. (2002) Weathering of ilmenite from granite and chlorite schist in the Georgia Piedmont. *Am. Mineral.* 87, 1616–1625.

Schwertmann U. (1983) Effect of pH on the Formation of Goethite and Hematite from Ferrihydrite. *Clays Clay Miner.* 31, 277–284.

Shannon R. D. (1976) Revised effective ionic radii and systematic studies of interatomic distances in halides and chalcogenides. *Acta Crystallogr.* A32, 751–767.

Soil Survey Staff (2017) Keys to soil taxonomy. *U. S. Dep. Agric. Wash. DC USA*, 639.

Stepanov A., A. Mavrogenes J., Meffre S. and Davidson P. (2014) The key role of mica during igneous concentration of tantalum. *Contrib. Mineral. Petrol.* 167, 1009.

Szilas K., Maher K. and Bird D. K. (2016) Aluminous gneiss derived by weathering of basaltic source rocks in the Neoarchean Storø Supracrustal Belt, southern West Greenland. *Chem. Geol.* 441, 63–80.

U.S.G.S (2022) *Niobium and Tantalum Statistics and Information*.

Vantelon D., Trcera N., Roy D., Moreno T., Mailly D., Guilet S., Metchalkov E., Delmotte F., Lassalle B., Lagarde P. and Flank A.-M. (2016) The LUCIA beamline at SOLEIL. *J. Synchrotron Radiat.* 23, 635–640.

Wall F., Williams C. T., Woolley A. R. and Nasraoui M. (1996) Pyrochlore from Weathered Carbonatite at Lueshe, Zaire. *Mineral. Mag.* 60, 731–750.

585 **Figure 1.** Geological context of the sampled profile: (a) location and geological map of the Pitinga
586 region (modified after Costi et al. 2000); (b) close-up of the sampling region indicating Nb
587 concentration in the different facies of the Madeira pluton. (c) Geological cross-section close to the
588 studied profile (modified after Bastos Neto et al. 2009).

589 **Figure 2.** Backscattered electron images of representative mineral assemblages in the parent granite:
590 (a) perthitic feldspars (Kfs) and local alteration of biotite (Bt); (b) EDS map of perthitic feldspars;
591 (c) zircon (Zrn), monazite (Mzn), ilmenite (Ilm) and xenotime (Xtm) around biotite; (d) ilmenite,
592 monazite and zircon within biotite.

593 **Figure 3.** Mineralogical and geochemical evolution of the studied profile: (a) log diagram of the
594 profile; (b) bulk mineralogy obtained by semi-quantitative analyses of X-ray diffraction patterns
595 (Ab: albite, Kfs: alkaline feldspar, Qz: quartz, Bt: biotite, Hem: hematite, Gt: goethite, Kln:
596 kaolinite, Ant: anatase, Gbs: gibbsite); (c) evolution of the concentration of major and (d) some
597 selected trace elements including HFSE with depth.

598 **Figure 4.** Backscattered electron images representative of the different horizons: (a) clayey mottled
599 horizon with quartz (Qz) and zircon (Zrn) grains dispersed in the kaolinite (Kln) matrix; (b) lateritic
600 horizon with scattered ilmenite (Ilm), zircon and Fe oxides in a gibbsite matrix; (c) bauxitic horizon
601 exhibiting large crystals of quartz distributed in a clay and gibbsite matrix on the scale of the thin
602 section; (d) stacking of kaolinite lamellae are associated to partially altered ilmenite. Numerous
603 micrometric crystals of Fe oxides are embedded in gibbsite (Gbs).

Figure 5. Evolution of the degree of weathering of the profile: (a) mass SiO_2–Al_2O_3–$Fe_2O_{3(T)}$ (SAF) ternary plot showing the degree of weathering experienced and the sampling depth; (b) correlations between the index of lateritization (IOL) and Nb, Sn, Th, Zr. Pearson correlation coefficient r is calculated for each element.

Figure 6. Mass fraction transport function τ obtained by mass-balance calculations as a function of depth for Nb, Ta, Zr, Hf, Sn, Y and Ti using Th as the immobile element of reference. Uncertainties on τ are between ± 1 and 20%.

Figure 7. Backscattered electron images of the Nb carriers of the parent granite: (a) inclusion of Nb-Y-bearing oxide (Nb-Y ox.) in Nb-bearing ilmenite (Nb ilm) that crystallized within biotite (Bt); (b) partial replacement of Nb-bearing ilmenite by Sc-rich ferrocolumbite (Sc-Clb); (c) mineralogical relationship between Nb-bearing ilmenite, monazite (Mnz), biotite and zircon (Zrn); (d) close-up on (c) showing the exsolution of Nb-Y-bearing oxide in Nb-bearing ilmenite. Niobium-bearing ilmenite is replaced by Nb-bearing pseudorutile (Nb pdrt).

Figure 8. Backscattered electron images of the different types of Nb-bearing ilmenite and Ti oxides found in the laterite: (a) EDS-SEM map of a heterogeneous crystal of Nb-bearing ilmenite (Nb Ilm) within kaolinite (Kln) in the bauxitic horizon; (b) Nb-bearing pseudorutile (Nb pdrt) crystal in the clayey mottled horizon displaying relics of Nb-bearing ilmenite and inclusions of columbite (Clb); (c) and (d) typical alteration features of Nb-bearing ilmenite in a kaolinitic matrix (Kln) in the bauxitic horizon; (e) type-1 Nb-bearing Ti oxide crystallized at the margins and between the kaolinite layers (Kln); (f) porous and fibrous type-1 Ti oxide crystallizing at the margins of kaolinite; (g) large crystal of pure Nb-bearing Ti oxide associated with monazite (Mnz) in the lateritic horizon; (h) euhedral type-2 Ti oxide intergrown with kaolinite.

Figure 9. Backscattered electron SEM images of Nb-bearing Fe oxides and columbite: (a) micron-size Nb-bearing Fe oxides in the clay matrix; (b) Zr-rich thorite probably mixed to Fe oxides overgrown by Nb-bearing Fe oxides; (c) euhedral crystal of columbite-(Mn) (Clb-Mn) in a kaolinite matrix (sample Col.1 in Table 4); (d) inclusion of ferrocolumbite (Clb-Fe) in ilmenite. The region of analysis of associated SEM-EDS spectra is indicated by the star symbols.

Figure 10. Fingerprint analysis of Nb L_3-edge XANES spectra with reference spectra: (a) columbite; (b) Nb-bearing Fe oxides (c) type-1 Nb-bearing Ti oxide; (d) type-2 Nb-bearing Ti oxide; (e) Nb-bearing ilmenite.

Figure 11. Evolution of the average Nb L_3-edge XANES spectra along the profile. Least-squares linear combination fitting of the altered horizons performed at the L_3-edge using Nb-bearing Fe oxides (Nb-Fe), Nb-bearing anatase (Nb-ant) and Nb-bearing ilmenite (Nb-ilm).

Figure 12. Evolution of the average Nb K-edge XANES spectra along the profile. Least-squares linear combination fitting of the lateritic horizons performed at the K-edge using Nb-bearing goethite (Nb-gt), Nb-bearing anatase (Nb-ant), Nb-bearing rutile (Nb-rt) and columbite (Clb). The spectrum of the granite cannot be reproduced in absence of relevant ilmenite spectrum, this phase being the main Nb host (Fig. S3).

Figure 13. Binary plots of the index of lateritization (IOL) versus mass fraction transport function τ. The increase of IOL is correlated with the decrease of τ for Ti, Zr and Hf (Pearson correlation coefficient: $r > 0.8$). Uncertainties on τ are between $\pm$ 1 and 20%.

Table 1. Representative compositions of Nb carriers from the parent granite (ILM: ilmenite, PDRT: pseudorutile, RT : rutile). Ti/(Ti+Fe) at% ratios between 0.6 and 0.7 are indicative of pseudorutile.

647 The sum of cations above 1 in rutile may arise from the interaction volume of the electron beam,

648 larger than the rutile size, which may also analyze biotite and ilmenite.

649

wt%	**ILM.1**	**ILM.2**	**ILM.3**	**ILM.4**	**PDRT.1**	**PDRT.2**	**PDRT.3**	**RT.1**	**RT.2**	**R**
TiO_2	52.66	50.17	48.76	50.69	61.93	67.06	65.62	78.84	73.19	7
MnO	10.09	7.60	7.49	9.55	0.78	0.47	0.68	0.38	0.42	0
FeO	35.76	39.20	40.29	37.38	28.76	25.73	27.12	18.04	20.15	2
Nb_2O_5	1.60	1.74	2.11	1.87	1.17	2.25	2.32	2.74	2.57	2
Ta_2O_5	0.11	0.38	0.22	0.31	0.08	0.08	0.18	0.22	0.34	0
Al_2O_3	/	0.22	/	/	/	/	/	/	/	/
SiO_2	0.08	1.30	0.03	0.11	0.70	0.91	1.36	1.25	1.75	2
Total	100.30	100.60	98.90	99.91	93.42	96.50	97.28	101.47	98.42	1
Ti/(Ti+Fe) at%	0.53	0.50	0.48	0.51	0.66	0.70	0.68	0.77	0.74	0
Structural formulae										
Ti	0.99	0.95	0.95	0.97	3.48	3.570	3.731	0.85	0.823	0
Mn	0.21	0.16	0.16	0.206	0.049	0.028	0.042	0.005	0.005	0
Fe	0.75	0.82	0.87	0.795	1.795	1.523	1.603	0.216	0.252	0
Nb	0.018	0.02	0.025	0.022	0.039	0.072	0.074	0.018	0.017	0
Ta	0.001	0.003	0.002	0.002	0.002	0.002	0.002	0.001	0.001	0
Al	/	0.007	/	/	/			/	/	/
Si	0.002	0.033	0.001	0.001	0.052	0.064	0.097	0.018	0.026	0
∑ Cations	1.971	1.993	2.008	1.996	5.417	5.259	5.549	1.108	1.124	1

wt%	ILM.1	ILM.2	ILM.3	ILM.4	PDRT.1	PDRT.2	PDRT.3	RT.1	RT.2	R

650

651 **Table 2.** Representative compositions of Nb-bearing ilmenite (Ilm) and type-2 Ti oxide from
652 lateritic horizons. Some analyses are far from 100 % due to contamination with neighboring phases.
653 Type-1 Ti oxide could not be analyzed using EPMA.

wt%	ILM.1	ILM.2	ILM.3	ILM.4	Type-2 Ti ox.1	Type-2 Ti ox.2	Type-2 Ti ox.3
TiO_2	52.92	53.08	53.93	55.47	98.60	92.39	96.45
MnO	4.86	6.33	4.89	4.05	/	/	0.04
Fe_2O_3	42.36	42.71	35.00	36.08	0.15	0.53	0.43
Nb_2O_5	0.79	0.91	1.27	1.01	1.42	3.69	2.13
Ta_2O_5	0.57	0.17	0.20	0.16	0.23	0.15	0.40
Al_2O_3	/	/	/	/	/	0.33	/
SiO_2	/	/	0.01	/	0.03	0.60	/
Total	101.5	103.20	95.30	96.78	100.43	97.69	99.45
Structural formulae							
Ti	0.995	0.982	1.049	1.059	0.988	0.956	0.981
Mn	0.103	0.132	0.107	0.087	/	/	0.000
Fe	0.885	0.879	0.757	0.766	0.002	0.006	0.005
Nb	0.009	0.010	0.015	0.012	0.009	0.023	0.013

wt%	ILM.1	ILM.2	ILM.3	ILM.4	Type-2 Ti ox.1	Type-2 Ti ox.2	Type-2 Ti ox.3
Ta	0.004	0.001	0.001	0.001	0.001	0.001	0.001
Al	/	/	/	/	/	0.005	/
Si	/	/	0.001	/	0.000	0.008	/
∑ Cations	1.996	2.004	1.930	1.925	1.000	0.999	1.000

654

655 **Table 3.** Representative compositions of Nb-rich goethite (Gt) from the lateritic horizons. The
656 presence of Si may result from the simultaneous analysis of kaolinite due to the interaction volume
657 of the electron, similar to the size of the analyzed Fe oxides crystals.

wt%	Gt.1	Gt.2	Gt.3	Gt.4	Gt.5	Gt.6	Gt.7
Fe_2O_3	78.03	73.72	78.34	85.60	86.92	75.43	81.10
TiO_2	1.75	1.31	0.16	2.01	0.76	0.99	1.10
Nb_2O_5	0.12	0.20	0.01	0.04	0.18	0.21	0.20
Al_2O_3	5.92	7.08	8.55	4.74	3.53	10.93	8.28
SiO_2	1.74	5.59	2.09	1.05	2.27	8.98	6.07
Total	87.56	87.89	89.15	93.45	93.67	96.53	96.76

658

659 **Table 4.** Representative compositions of columbite-(Mn) (Col) from the Pitinga weathering profile.
660 The composition of Sc-rich columbite could not be determined by EPMA due to their sub-
661 micrometric size (Fig. 9d).

wt%	Col.1	Col.2	Col.3
FeO	5.76	9.10	17.92
MnO	13.68	10.40	1.97
Al_2O_3	0.12	0.05	/
Nb_2O_5	70.82	71.27	73.27
TiO_2	0.22	0.87	4.39
Ta_2O_5	7.50	6.95	2.88

wt%	Col.1	Col.2	Col.3
Total	98.12	98.63	100.42
Structural formulae			
Fe	0.298	0.464	0.848
Mn	0.717	0.537	0.094
Al	0.009	0.003	0.000
Nb	1.980	1.965	1.874
Ti	0.010	0.040	0.187
Ta	0.126	0.115	0.044
A site	2.117	2.121	2.105
B site	1.024	1.005	0.942

662

663 **Table 5.** Comparison of the average Nb speciation between the L_3- and K-edges obtained by linear
664 combination fitting procedures. Qualitative Nb speciation as observed using SEM is also indicated.
665 Relative abundances range from trace (o) to dominant (+++) phases.

Technique	Sample	Nb speciation				
SEM		**Ilmenite**	**Rutile**	**Anatase**	**Goethite**	**Columbite**
	Bauxitic horizon	**+**	**/**	**++**	**+**	**+**
	Lateritic horizon	**+**	**/**	**++**	**+**	**o**
	Clayey mottled horizon	**++**	**/**	**++**	**o**	**o**
	Biotite granite	**+++**	**+**	**/**	**/**	**o**
Nb L_3-edge		**Ilmenite**	**Rutile**	**Anatase**	**Fe oxide**	**Columbite**
	Bauxitic horizon	20 %	/	20 %	60 %	/

	Lateritic horizon	20 %	/	30 %	50 %	/
	Clayey mottled horizon	60 %	/	40 %	/	/
Nb K-edge		**Ilmenite/Ti oxide**			**Goethite**	**Columbite**
	Duricrust horizon	/			50 %	50 %
	Bauxitic horizon	25 %			60 %	15 %
	Lateritic horizon	50 %			50 %	/
	Clayey mottled horizon	100 %			/	/

666

667

668 **Declaration of interests**

669

670 x The authors declare that they have no known competing financial interests or personal
671 relationships that could have appeared to influence the work reported in this paper.

672

673 ☐The authors declare the following financial interests/personal relationships which may be considered as
674 potential competing interests:

675

676

677